Mesh size effects on fracture locus of high strength bolts
A mesoscale critical equivalent plastic strain (MCEPS) approach

Li, Jie; Xin, Haohui; Correia, José A.F.O.; Berto, Filippo; Zhao, Bingzhen; Bo, Yanwei; Veljkovic, Milan

DOI
10.1016/j.engfailanal.2022.106385

Publication date
2022

Document Version
Final published version

Published in
Engineering Failure Analysis

Engineering Failure Analysis 138 (2022) 106385

Contents lists available at ScienceDirect

Engineering Failure Analysis

journal homepage: www.elsevier.com/locate/engfailanal

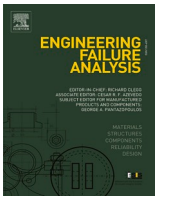

Mesh size effects on fracture locus of high strength bolts: A mesoscale critical equivalent plastic strain (MCEPS) approach

Jie Li [a], Haohui Xin [a,*], José A.F.O. Correia [a,b,c], Filippo Berto [a,d], Bingzhen Zhao [e], Yanwei Bo [f], Milan Veljkovic [c]

[a] Department of Civil Engineering, Xi'an Jiaotong University, Xi'an 710116, China
[b] CONSTRUCT & INEGI, Faculty of Engineering, University of Porto, 4200-465 Porto, Portugal
[c] Faculty of Civil Engineering and Geosciences, Delft University of Technology, Netherlands
[d] Department of Mechanical and Industrial Engineering, Norwegian University of Science and Technology (NTNU), Norwegian, Norway
[e] Future City Innovation Technology Co., Ltd., Shaanxi Construction Engineering Holding Group, Xi'an 710116, China
[f] Shaanxi Steel Structures Construction Engineering Co., Ltd., Xi'an 710116, China

ARTICLE INFO

Keywords:
High strength bolts
Ductile fracture
Finite element simulation
Mesh size sensitivity

ABSTRACT

With the improvement of computational capability, finite element simulation is an increasingly practical method to accurately predict the ultimate capacity and ductile fracture behavior of high-strength bolts. However, the mesh size affects the results of FE simulations but related research on mesh size effects is relatively limited. In the present contribution, the mesoscale critical equivalent plastic strain (MCEPS) is used as a failure index for calibrating the parameters of ductile fracture locus of high-strength bolts with different mesh sizes. The identified fracture locus is compared with a large bulk of experimental data taken from the previously published literature. The results showed that mesh size can have high effects on the calibrated parameters of the plastic constitutive relationship after necking and ductile fracture locus of high-strength bolts.

1. Introduction

Bolts are widely used to connect different steel components, which are critical to the stability and integrity of the steel structural system [1-3]. In the past few years, high-strength bolts are favored by the infrastructure sector because of their economical and functional advantages. However, with the application of high-strength bolts, the joint regions between connected components also become narrow [4,5]. To ensure the overall integrity of the structure and to make sure the efficient transferring of the load between joint and beam/column, it is necessary to evaluate the ultimate capacity and ductile fracture behavior of high-strength bolts. The first step is to identify the reliable material parameters of the plastic constitutive relationship and ductile fracture locus.

The fracture of bolts can be classified into overload, fatigue, and delayed fracture [6]. The fracture of axial-connected bolts of the thin-walled cylinder [7] is a typical case of fracture. Overload fracture occurs when the bolt is subjected to excessive load or deformation, this kind of fracture will be disastrous in the high-rise or long-span structures. Those structures are subject to progressive collapse due to failure of connections, and such collapse often occurs where local failure eventually leads to overall damage. The collapse of the Ronan Point apartment building in 1968 [8] and the World Trade Center building in New York in 2001 [9] were both progressive collapses. The Institution of Structural Engineers states that the vulnerability of progressive structures is "directly related

* Corresponding author.
E-mail address: xinhaohui@xjtu.edu.cn (H. Xin).

https://doi.org/10.1016/j.engfailanal.2022.106385
Received 6 January 2022; Received in revised form 24 April 2022; Accepted 29 April 2022
Available online 14 May 2022

Table 1
Comparison of mechanical properties for high-strength bolts.

	Performance grade	Tensile strength/*MPa*
GB/T 3098.1	8.8	830
	9.8	900
	10.9	1040
	12.9	1220
AISC-360	Group A	620
	Group B	780
	Group C	1040
EC3	8.8	800
	10.9	1000

Where: GB/T 3098.1 used the minimum value of ultimate tensile strength as the base data, AISC-360 proposed the nominal tensile strength, and EC3 used the nominal value of ultimate tensile strength as the base data.

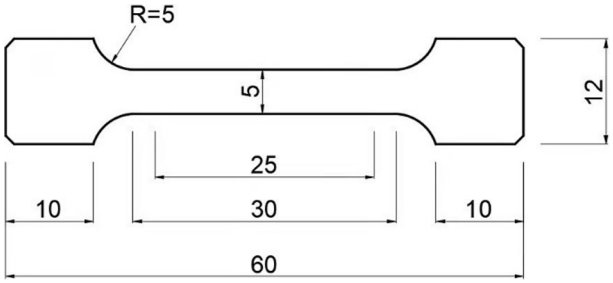

Fig. 1. The geometry of tensile bolt model (dimensions in mm).

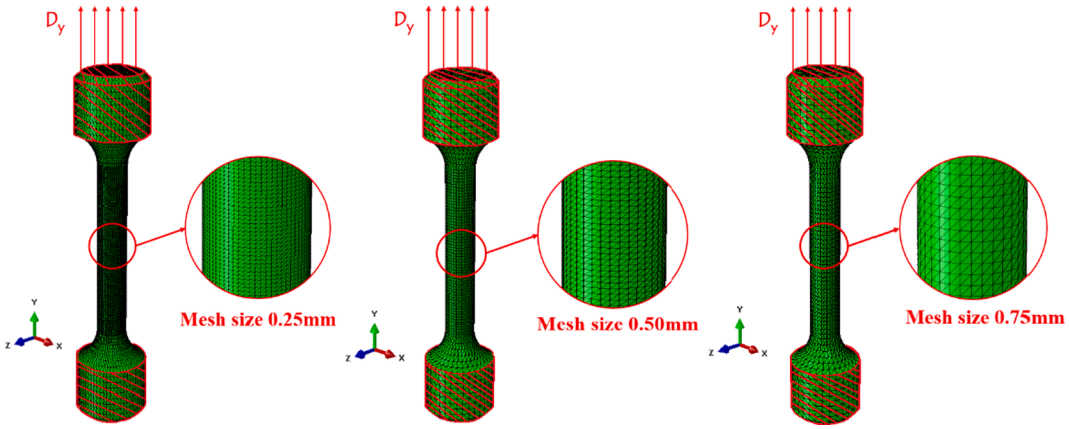

Fig. 2. Mesh size of finite element model and boundary condition.

to the strength, ductility, and hence the energy absorption capacity of the connections between the main structural elements" [9]. Local damage due to bolt fracture increases the risk of progressive collapse of the structure. External loads affect different types of fracture, so an accurate assessment of the ultimate capacity performance and fracture behavior of the bolts is required as the first step in evaluating the mechanical properties of the bolt.

Many of the current international design standards have allowed the utilization of high-strength bolts [10-13]. In China, GB/T 3098 [11] gave four grades of high-strength bolts, including 8.8, 9.8, 10.9, and 12.9. Different methods are used to control the content of chemical components such as C, P, S, and B to obtain the high-strength bolts. For example, Chinese specifications recommend using 35, 40B, and 45 steel materials for processing grade 8.8 bolts, while for grade 10.9 bolts, 20MnTiB and 35VB steel materials are recommended for processing. In Europe, Eurocode 3 [12] specified the ultimate tensile strength of grade 8.8 and 10.9 high-strength bolts. Different from other standards, American specification AISC-360 [13] divided high-strength bolts into three groups A, B, and C according to material strengths. Table 1 compared the mechanical properties of different design specifications for high-strength bolts.

In the past few years, the ultimate capacity and fracture behavior were investigated by experimental methods. Sterling & Fisher [14], Nair et al. [15], and Amrine & Swanson [16] tested the tensile performance of ASTM-A490 bolts and discussed the effects of

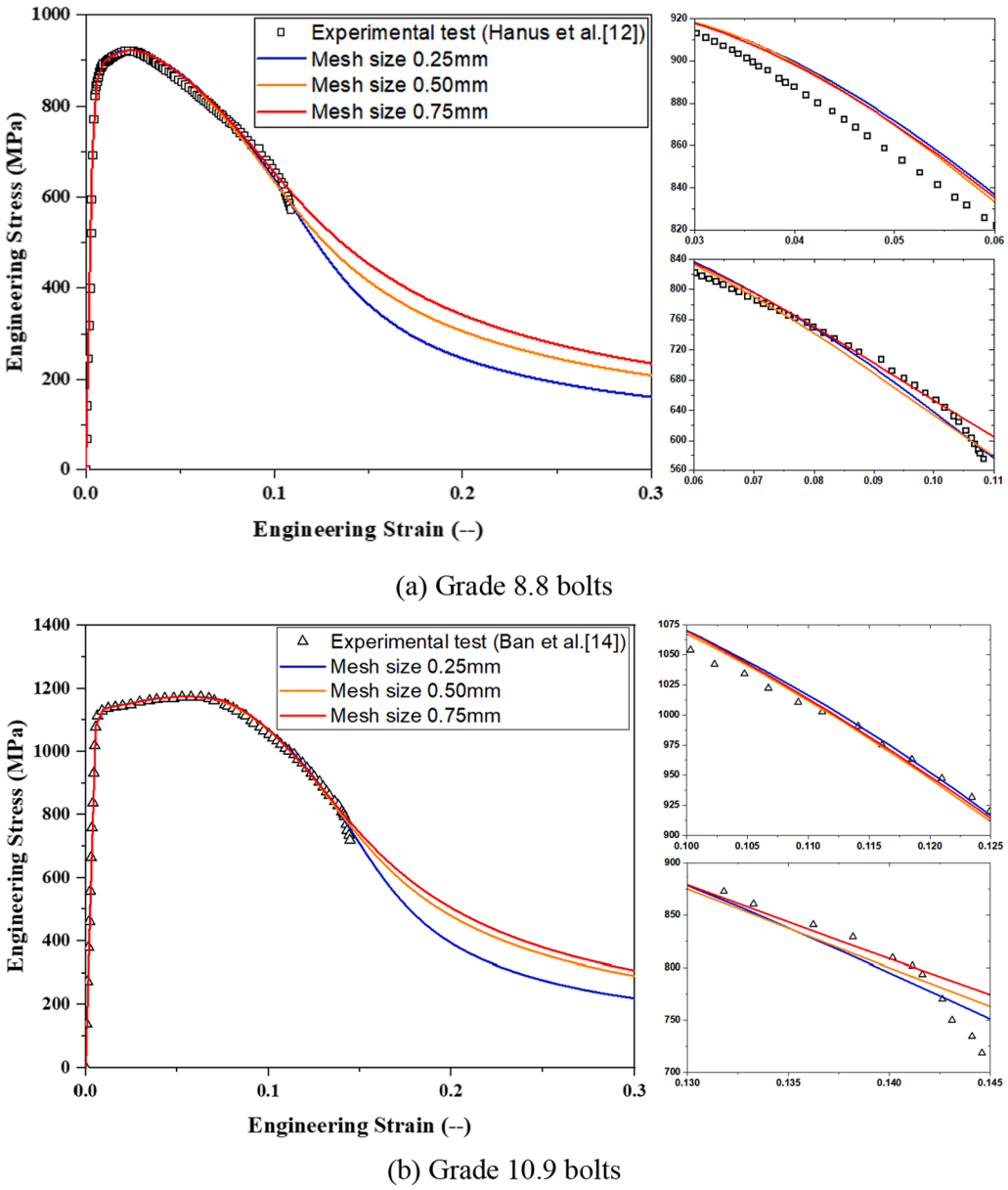

Fig. 3. Comparisons between FE (without damage) and experimental results under different mesh sizes.

carriable pretension on the tension bolted connections. Pang et al. [17] tested the tensile performance of grade 8.8, 10.9, and 12.9 high strength bolts, where the stress–strain response of different grades of bolts at different temperatures is summarized. Li et al.[19] investigated the properties of grade 12.9 high strength bolts, where the result showed that grade 12.9 structural bolts exhibited satisfactory ultimate loading capacities under various statuses. After comparing with European, American, and Australian standards (EC3, AISC-360, and AS 4100), the results showed that current international design standards for grade 12.9 bolts are either too conservative (EC3) or unsafe (AS4100 and AISC-360). Hanus et al. [20] deeply investigated the behavior of grade 8.8 bolts with experimental test and model, concluded that a heating–cooling cycle has a significant effect on the mechanical behavior of grade 8.8 bolts.

Over the past few years, many researchers have investigated the behavior of high-strength bolts through finite element analyses. Hedayat et al. [21] and D'Aniello et al. [22] used a simplified model to evaluate the mechanical properties of bolts. Mersch et al. [23] predicted the failure of threaded bolts using geometrically-simplified finite element models. Song et al. [24] simulated the fracture of stainless-steel bolts with the element deletion method by the Lee-Wierzbicki model, the load-deformation behavior under ultimate strength matched well with experimental data. Schauwecker et al. [25] used the GISSMO damage model to study the failure of bolts.

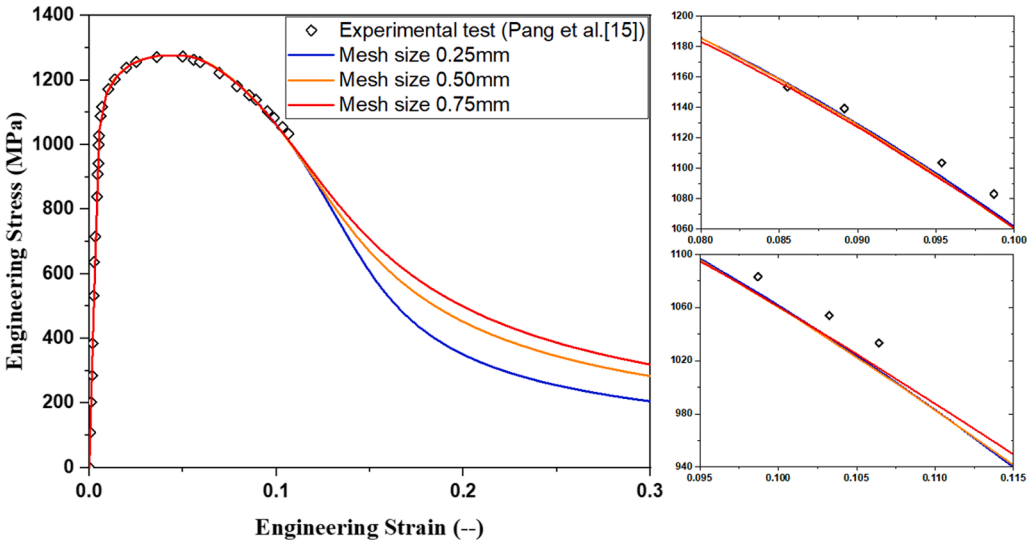

(c) Grade 12.9 bolts

Fig. 3. (*continued*).

Xin et al. [26] simulated numerially the ductile fracture of grade 10.9 bolts subject to combined tension-shear actions, twin-shear actions, and combined tension-twin shear actions, and compared the ultimate resistance predicted with the existing design provisions.

The most common method for simulating the fracture of bolts is the uncoupled fracture model with the element deletion method. The advantage of the uncoupled fracture model with the element deletion method is the convenience to calibrate the fracture parameters. While the disadvantage of the element deletion method is a high dependence on the mesh at the fracture region, an inaccurate result will be produced due to the deletion of cells. Noted that the mesh size of the model can have a high impact on the final results of the simulations. While the discussions on the mesh size effects of numerical modeling for high strength bolts are relatively limited.[27-29] In this paper, the fracture locus of three types of bolts, namely grade 8.8 [17], grade 10.9 [18], and grade 12.9 [19], are calibrated based on the mesoscale critical equivalent plastic strain (MCEPS) approach proposed recently by the authors [30,31]. Three various mesh sizes (0.25 mm, 0.50 mm, and 0.75 mm) are employed to observe the effects on material parameters of ductile fracture locus. The calibration process of ductile fracture of high-strength bolts is divided into two stages [32]: ①Identify the constitutive plastic relationship for the rate-independent non-linear isotropic J2 hardening model; ②Identify parameters of fracture strain under multiaxial stress states using MCEPS [3031] and Lou-Huh model [33]. The plasticity curves of three grades of high-strength bolts are compared at different mesh sizes.

2. Plastic flow stress

The geometry of the high-strength bolt is illustrated in Fig. 1. This section presented the material parameter calibration of the coupled plastic-damage stage. The FE model and boundary conditions are shown in Fig. 2. One side is fixed while the other side is used for loading. To eliminate the influence of element type on the calibrated results, the mesh type is fixed as tetrahedron by solid element C3D10. Mesh sizes of 0.25 mm, 0.50 mm, and 0.75 mm are used to investigate its effect on the plastic constitutive relationship and fracture strain. The target time increment is controlled to be $1 \times e^{-5}$ when using the explicit solver to model quasi-static loading.

The whole uniaxial plastic relationship of high-strength bolts is divided into three stages in this paper: elastic stage, plastic stage, and coupled plastic-damage stage [32]. The third stage is further decomposed into two zones by damage initiation point as the plastic-dominated zone and the damage-dominated zone. The calibration of the true stress-plastic strain relationship of each stage is based on the method previously proposed by ref. [32]. W is a weight constant ($0 \le W \le 1$) which is calibrated in the plastic-dominated zone by comparing the engineering stress–strain curve and the test results. As expressed in Equation (1), the weighted function is used to predict the true stress after necking.

$$\overline{\sigma}^{neck} = \overline{\sigma}_u \left[W\left(1 + \overline{\varepsilon}^p - \overline{\varepsilon}_u^p\right) + (1 - W)\left(\frac{\left(\overline{\varepsilon}^p\right)^{\overline{\varepsilon}_u^p}}{\left(\overline{\varepsilon}_u^p\right)^{\overline{\varepsilon}_u^p}}\right) \right] \tag{1}$$

Where: $\overline{\varepsilon}_u^p$ is the corresponding plastic strain when the true stress without considering necking and damage effects reached the peak.

The parameter B of damage law is identified in the damage-dominated zone of the coupled plastic-damage stage. The damage evolution law is expressed in Equation (2), and true stress in the damage-dominated zone could be obtained through Equation (3).

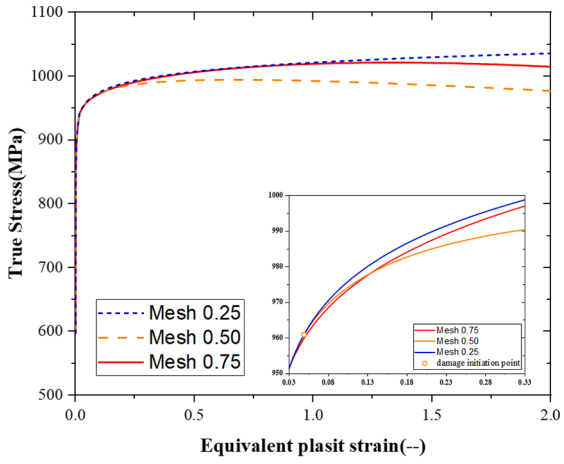

(a) Grade 8.8 bolts

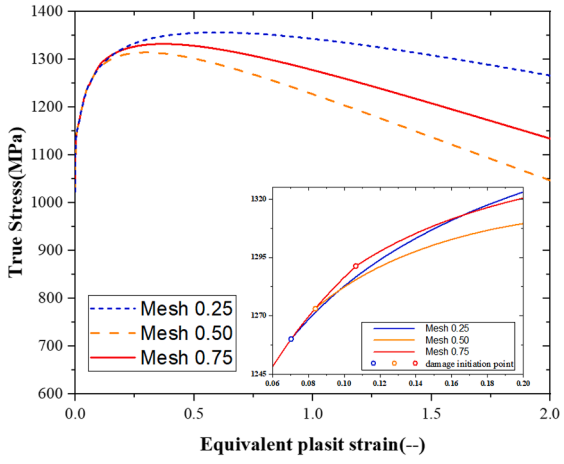

(b) Grade 10.9 bolts

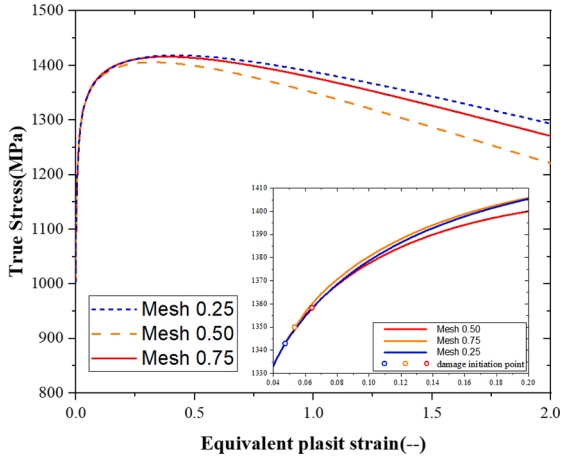

(c) Grade 12.9 bolts

Fig. 4. Relationship between mesh size and uniaxial true stress–strain curves without considering the damage.

$$d = \begin{cases} 0, \bar{\varepsilon}^{p} < \bar{\varepsilon}^{p}_{d-i} \\ 1 - exp[-B(\bar{\varepsilon}^{p} - \bar{\varepsilon}^{p}_{d-i})], \bar{\varepsilon}^{p} \geq \bar{\varepsilon}^{p}_{d-i} \end{cases} \tag{2}$$

Table 2
Summary of plastic constitutive relationship parameters.

	$\overline{\sigma}_u$(MPa)	$\overline{\varepsilon}^p_u$	Mesh 0.25 mm			Mesh 0.50 mm			Mesh 0.75 mm		
			W	$\overline{\varepsilon}^p_{d-i}$	B	W	$\overline{\varepsilon}^p_{d-i}$	B	W	$\overline{\varepsilon}^p_{d-i}$	B
G8.8	943.94	0.0203	0	–-	–-	0	0.0489	0.03	0.2	0.0289	0.16
G10.9	1247.15	0.0592	0	0.0704	0.1	0	0.0839	0.20	0	0.1065	0.16
G12.9	1336.41	0.0421	0	0.0473	0.1	0	0.0532	0.13	0	0.0642	0.11

Where: $\overline{\sigma}_u$ is the ultimate tensile strength for high-strength bolts.

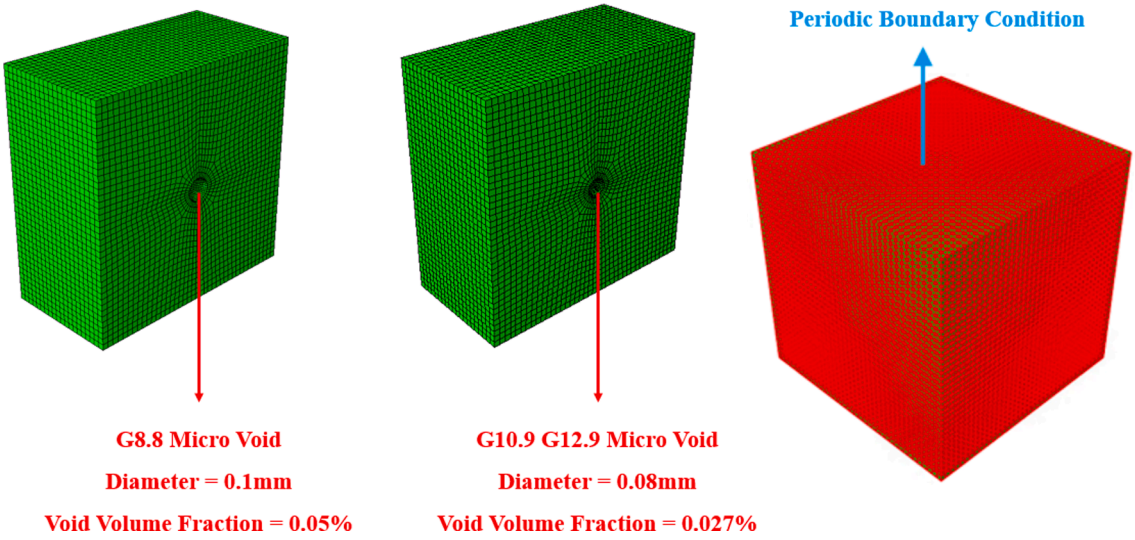

Fig 5. Illustration of the unit cell.

$$\overline{\sigma} = (1-d)\overline{\sigma}^{neck} \tag{3}$$

Where: $\overline{\varepsilon}^p_{d-i}$ is strain point that divided plastic-dominated zone and damage-dominated zone.

As shown in Fig. 3, a good agreement is observed between the experiment test and FE simulation. The curves are the same for the three different mesh sizes in the elastic and plastic phases; while diverging from the coupled plastic-damage stage. This is due to the plastic response after necking being highly dependent on the mesh. The bifurcation of the curves becomes more pronounced from the damage-dominated zone. The reason is the variability of maximum equivalent plastic strain $\overline{\varepsilon}^p_{d-i}$ and damage parameter B which calibrated at this stage [34]. After the start of necking, there is a slight difference between the three curves, where the curve of 0.25 mm mesh size is at the top and the curve of 0.75 mm mesh size is at the bottom, after the appearance of uncoupled deformation (without considering damage), it can be observed that the curves drop faster when the mesh size is smaller. The curve corresponding to 0.25 mm drops to the minimum, while the curve corresponding to 0.75 mm is instead above the other two curves. Taking the Grade 8.8 high-strength bolt as an example, the engineering stress of the blue curve (mesh size 0.25 mm) is the largest when the engineering strain is at 0.03–0.06, followed by the orange (mesh size 0.50 mm) line, and the red (mesh size 0.75 mm) line has the smallest value of engineering stress. However, when the strain reaches about 0.07, the trend starts to change, it is obvious that the blue curve is at the bottom while the red one is at the top when the engineering strain reaches 0.1. The same tendency is observed for bolts of Grade 10.9 and 12.9, as shown in Fig. 3.

Fig. 4 shows the relationship between mesh size and uniaxial true stress-equivalent plastic strain curves without considering the damage. In the initial stage, there is not a clear distinction between the three curves. As the start of necking, the curve with a 0.25 mm mesh size is the highest among the three curves, while the curve for 0.5 mm is the lowest. This is because the maximum equivalent plastic strain $\overline{\varepsilon}^p_{d-i}$ and the damage factor used in the 0.25 mm mesh size calibration is the smallest of the three. Although the maximum equivalent plastic strain $\overline{\varepsilon}^p_{d-i}$ obtained for the 0.5 mm mesh size is not the largest, it has the largest damage parameter B of the three, which reduces the true stress in the damage-dominated zone. This can illustrate that the effect of mesh size starts from the coupled plastic-damage stage. The calibrated parameters for the plastic stage and coupled plastic-damage stage are summarized in Table 2.

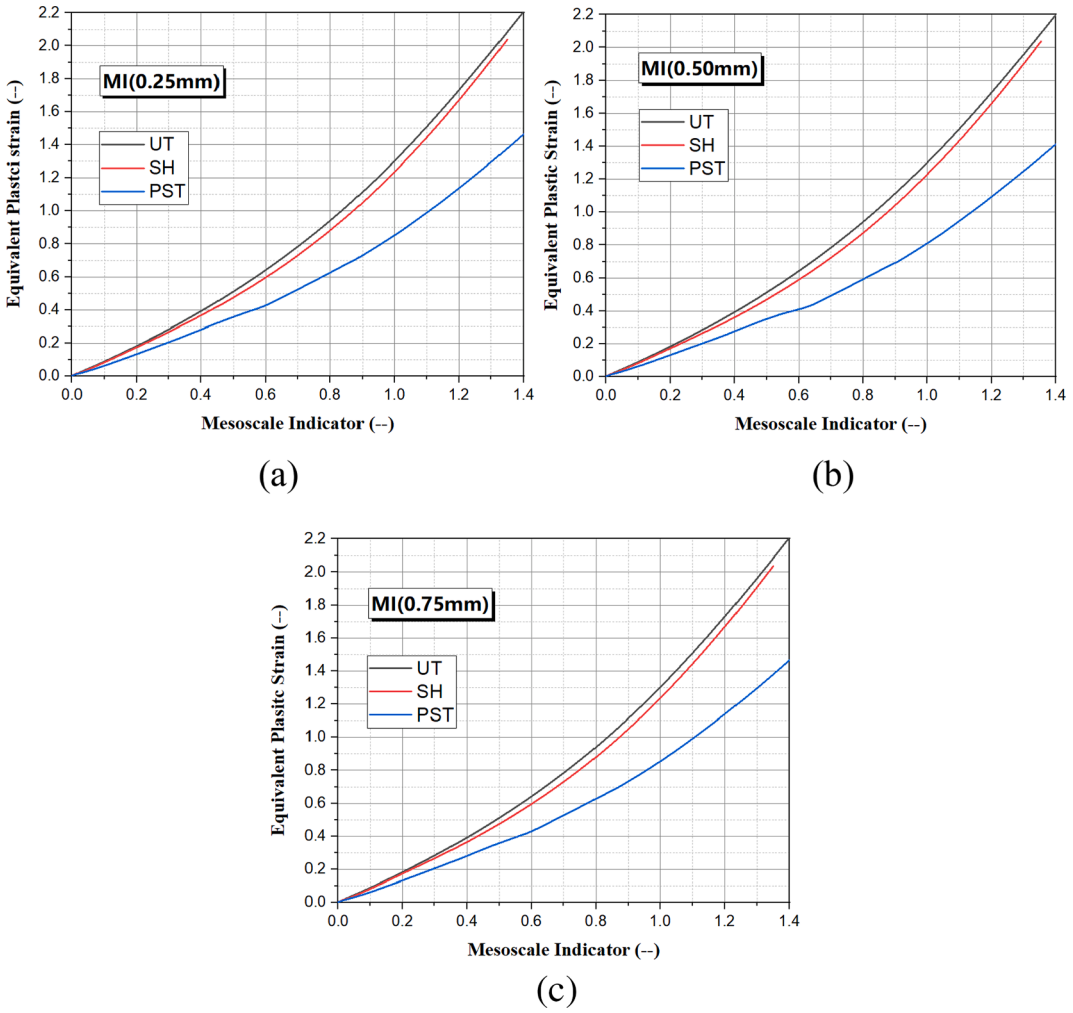

Fig 6. Mesoscale indicator evolution along with the equivalent plastic strain for Grade 8.8 high-strength bolt.

3. Computational homogenization

The cubic with a void in the center is assumed to be the unit cell[31]. As shown in Fig. 5, the diameter of void spheres is determined depending on the composition of the three grades of bolt materials. The diameter and porosity of the central void are calculated by Equation (4), [35]. The void diameter of grade 8.8 bolts is 0.1 mm, and the corresponding void volume fraction is 0.05%. The void diameter of both grade 10.9 and 12.9 bolts is 0.08 mm because the chemical composition of the two materials is similar, and the void volume fraction is 0.027%:

$$f_0 = 0.054\left[\%\mathrm{S}(wt) - \frac{10^{-3}}{\%\mathrm{Mn}(wt)}\right] + 0.055\%\mathrm{O}(wt) \tag{4}$$

where: f_0 is the porosity of the whole unit cell; $\%\mathrm{S}(wt)$ is the percentage content of the chemical element sulfur; $\%\mathrm{Mn}(wt)$ is the percentage content of manganese; and $\%\mathrm{O}(wt)$ is the percentage content of oxygen in the high-strength bolt. The void diameter can be obtained from the calculated porosity of the unit cell.

The ductile fracture of the macroscale is due to the nucleation, growth, and coalescence of micro-voids in microscale. MCEPS on the microvoid surface is defined as the failure indicator that the behavior of macro-scale under complex stress status is obtained by virtual loading at the microscopic scale. It is assumed that the MCEPS of the unit cell is kept constant when the material is exposed to multiaxial loading. Homogenized equivalent strain is selected in this paper as the failure index, the expression is as Equation (5),[31].

$$MI = \int_{\Gamma_v} \bar{\varepsilon}^p d\Gamma \tag{5}$$

The micro void deformation of the unit cell under various loading conditions is simulated, including uniaxial tension (UT), pure

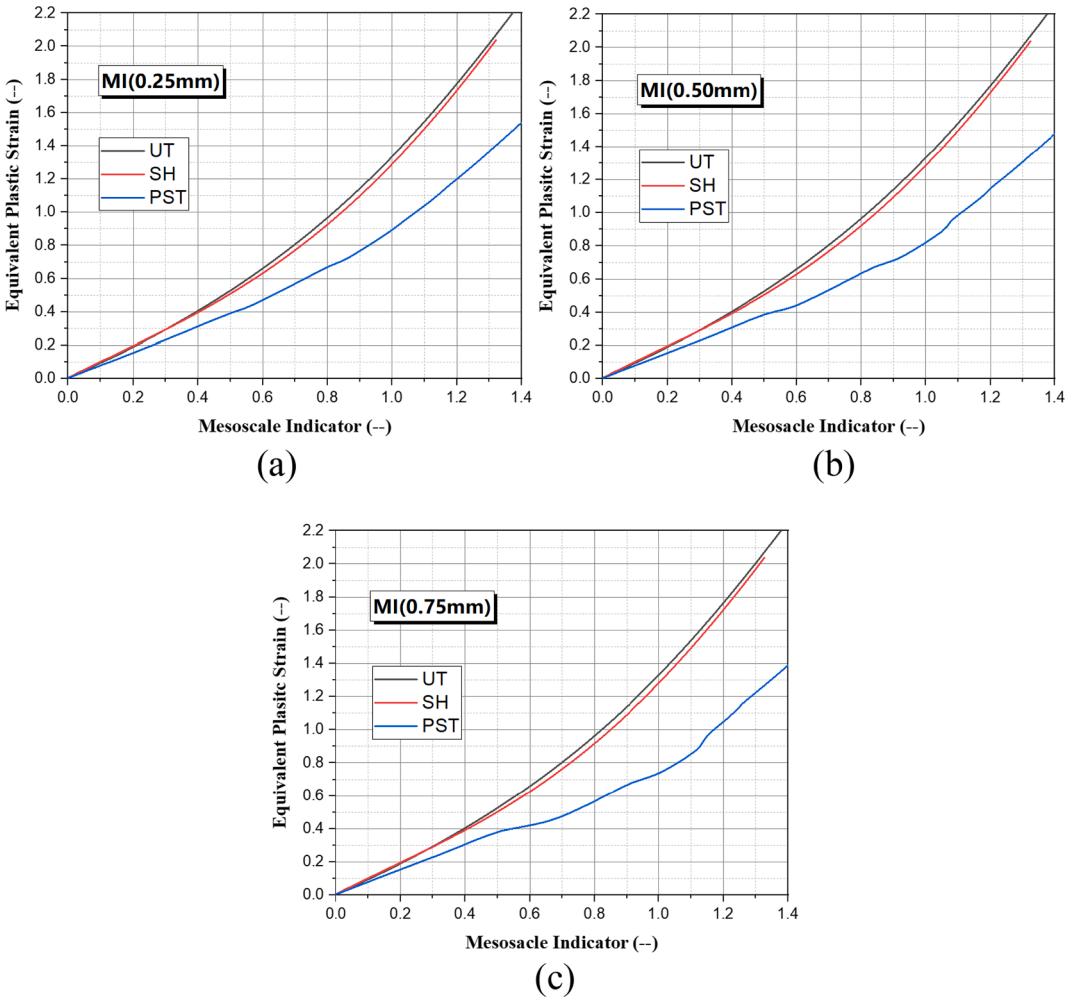

Fig 7. Mesoscale indicator evolution along with the equivalent plastic strain for Grade 10.9 high-strength bolt.

shear (SH), and plane strain tension (PST). The MI evolution along with the macro equivalent plastic strain is shown in Figs. 6-8. The equivalent plastic strain with the same MI value is extracted from the uniaxial tension (UT), pure shear (SH), and plane strain tension (PST) curves in Figs. 6-8.

As shown in Fig. 9, two groups of curves were obtained which included SH/UT and PST/UT, each with three mesh sizes of 0.25 mm, 0.50 mm, and 0.75 mm. The fracture strain exposed to uniaxial tension (UT) is determined. The ratios of fracture strain, SH to UT, and PST to UT are further obtained, by a seven-term polynomial expression which is fitted as the relationship between strain ratio and fracture strain exposed to uniaxial strain, as expressed in Equation (6)[31]. It can be observed that compared to curve SH/UT, the curve PST/UT changes more significantly at different mesh sizes. Table 3 is a summarization of fitted coefficients.

$$r_x = \sum_{i=1}^{7} \xi_i (\bar{\varepsilon}^p_{UT})^{i-1} x = \mathrm{SH/UT"}, PST/UT'' \tag{6}$$

Where: r_x is the fracture strain ratio between pure shear (SH) / plane strain tensile (PST) and uniaxial tensile loading (UT); ξ_i is the coefficient of polynomial expression; $\bar{\varepsilon}^p_{UT}$ is the fracture strain exposed to uniaxial tension.

4. Identification of fracture locus

The uncoupled models were adopted to simulate the ductile of high strength bolt. The fracture strain is a function of stress triaxiality and Lode angle parameters, and given by Equation (7) [38]:

$$\bar{\varepsilon}^p_f = C_3 \left(\frac{\sqrt{\bar{L}^2+3}}{2}\right)^{C_1} \left[\frac{1}{1+C}\left(\bar{\eta} + \frac{3-\bar{L}}{3\sqrt{\bar{L}^2+3}} + C\right)\right]^{-C_2} \tag{7}$$

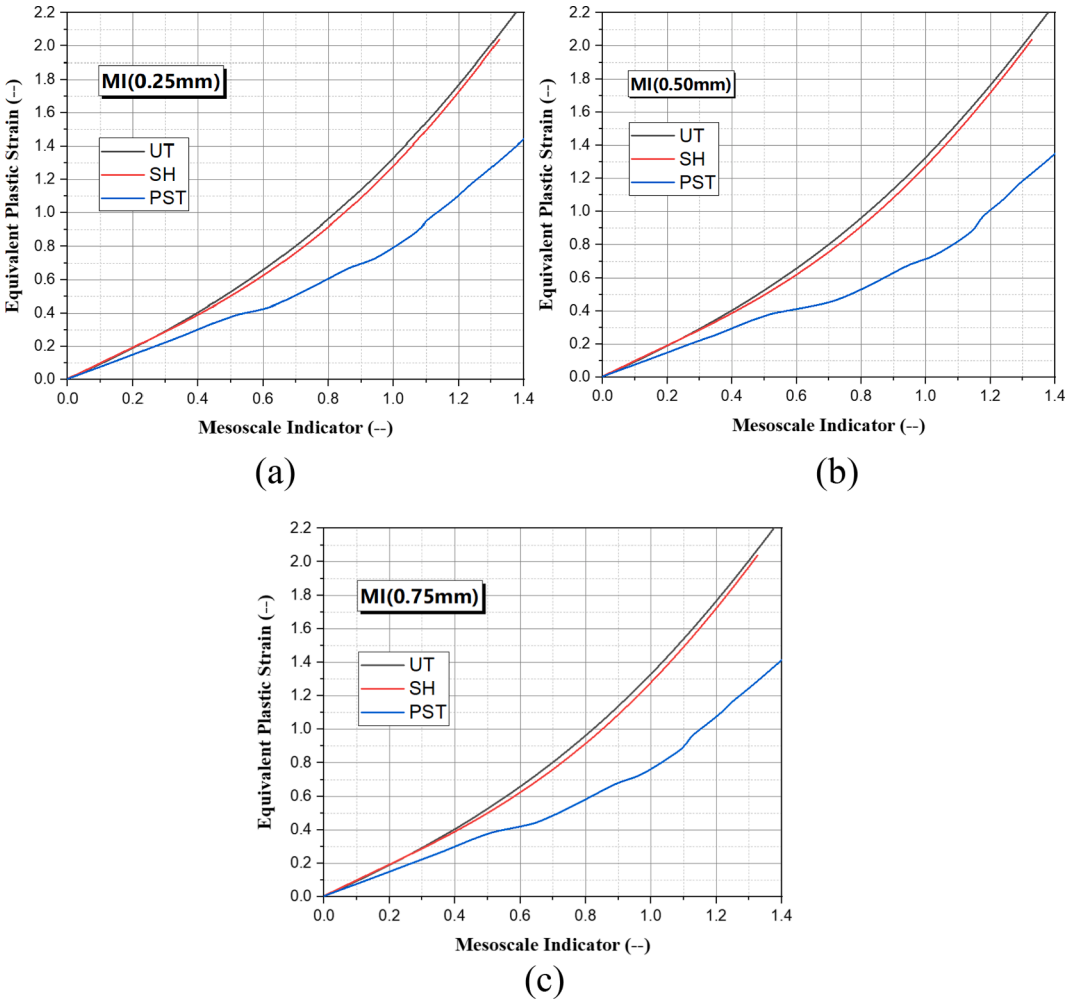

Fig. 8. Mesoscale indicator evolution along with the equivalent plastic strain for Grade 12.9 high-strength bolt.

where: $\bar{\eta}$ and $\bar{L}$ are the stress triaxiality and Lode Angle parameters averaged over the loading history to consider the non-proportional loading effects, respectively. The expressions for C_1, C_2 and C_3 are indicated in Equations (8)-(10)[38].

$$C_1 = \log_{(\frac{2}{\sqrt{3}})}\left[\frac{\bar{\varepsilon}^p_{UT}\left(\frac{1}{\sqrt{3}}+C\right)}{\bar{\varepsilon}^p_{SH}\left(\frac{2}{\sqrt{3}}+C\right)}\right]^{-C_2} \tag{8}$$

$$C_2 = \log_{\frac{\frac{1}{\sqrt{3}}+C}{\left(\frac{2}{\sqrt{3}}+C\right)}}\left(\frac{\bar{\varepsilon}^p_{PST}}{\bar{\varepsilon}^p_{SH}}\right) \tag{9}$$

$$C_3 = \bar{\varepsilon}^p_{UT} \tag{10}$$

The ratios of SH to UT and PST to UT are obtained in the previous section. The values of C_1, C_2, and C_3 can be calculated accordingly for different bolt grades and different mesh sizes. The fracture strain exposed to uniaxial tensile could be determined through the calibration by comparing the FE result against the experimental results. Comparisons of engineering stress-engineering strain curves and test values for three mesh sizes of grade bolts 8.8, 10.9, and 12.9 are shown in Fig. 10. Interestingly, the engineering stress in the necking stage of the curve during the calibration of the fracture locus is slightly greater than the experimental data. Dynamic Explicit Solver is used to identify the fracture locus of the high-strength bolts, but the Static General Solver is used for the calibration of the plastic parameters. The degree of curve deviation depends on the mesh size, it could be found that finer size has a higher deviation. For grade 8.8 bolts, the maximum difference between the FE model and experimental results is about 5%, grade 10.9 is 4.4%, and 4.2% for grade 12.9 high strength bolts. In addition, it is noted that the curve of 0.75 mm size drops fastest after the fracture.

The parameter of fracture strain $\bar{\varepsilon}^p_f$ exposed to uniaxial loading is summarized in Table 4. When the mesh size is 0.25 mm, the corresponding fracture strain for grade 8.8 bolts is 0.82, then it rises to 0.85 when the mesh size is 0.75 mm. The fracture strain for

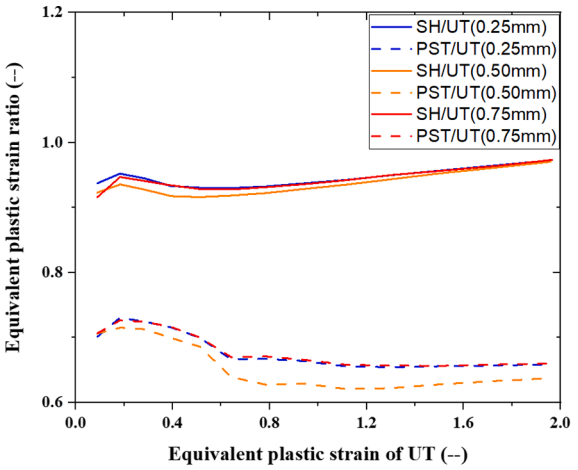

(a) Grade 8.8 bolts

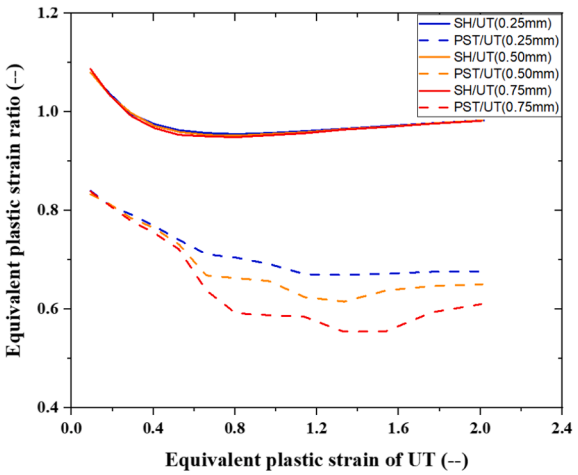

(b) Grade 10.9 bolts

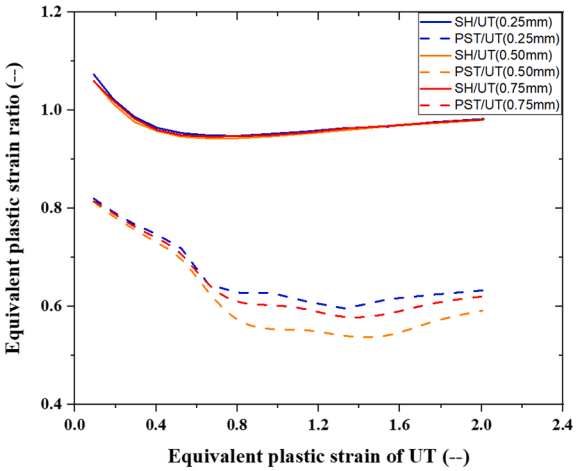

(c) Grade 12.9 bolts

Fig. 9. Equivalent plastic strain ratio evolution with stretching exposed to pure tension.

Table 3
Parameters of damage model and fracture strain at different stress status with a different mesh size.

Grade	Mesh size (mm)	MI	ξ_1	ξ_2	ξ_3	ξ_4	ξ_5	ξ_6	ξ_7
G8.8	0.25	$r_{SH/UT}$	−0.1703	1.1123	−2.8076	3.4077	−1.9745	0.4609	0.9117
		$r_{PST/UT}$	−0.237	1.6255	−4.3777	5.8105	−3.837	1.0393	0.6356
	0.50	$r_{SH/UT}$	−0.1565	1.0121	−2.5218	3.0035	−1.6847	0.3766	0.9028
		$r_{PST/UT}$	−0.0624	0.5488	−1.8609	3.0335	−2.3398	0.637	0.6641
	0.75	$r_{SH/UT}$	−0.2344	1.5553	−4.0077	5.0176	−3.0834	0.8264	0.866
		$r_{PST/UT}$	−0.189	1.3025	−3.5288	4.719	−3.1402	0.846	0.6522
G10.9	0.25	$r_{SH/UT}$	−0.1578	0.6747	−0.9012	0.0606	0.8685	−0.7277	1.1411
		$r_{PST/UT}$	0.1385	−0.5463	0.7389	−0.3773	0.1419	−0.2739	0.863
	0.50	$r_{SH/UT}$	−2.597	9.9841	−14.903	10.803	−3.7517	0.4274	0.9805
		$r_{PST/UT}$	0.7196	−1.7766	0.3336	2.3498	−2.1925	0.5122	0.8212
	0.75	$r_{SH/UT}$	−1.5996	5.8038	−7.8105	4.3701	−0.2887	−0.6697	1.1489
		$r_{PST/UT}$	−9.1316	27.509	−29.167	12.893	−2.1412	−0.2348	0.8715
G12.9	0.25	$r_{SH/UT}$	−1.097	3.798	−4.710	2.086	0.477	−0.737	1.1366
		$r_{PST/UT}$	−1.2468	−0.491	8.4639	−11.091	5.3598	−1.261	0.9003
	0.50	$r_{SH/UT}$	−0.0088	−0.081	0.5906	−1.3839	1.5736	−0.8712	1.129
		$r_{PST/UT}$	3.2687	−16.077	29.972	−26.156	10.771	−2.1738	0.9438
	0.75	$r_{SH/UT}$	−0.0094	0.0105	0.1915	−0.7407	1.1127	−0.7335	1.1206
		$r_{PST/UT}$	−0.0982	0.7025	−2.0272	2.9397	−2.0065	0.2837	0.7985

grade 10.9 bolts is 0.7 when the mesh size is 0.25 mm, when the mesh size increases to 0.75 mm, the corresponding fracture strain increases to 0.89. For grade 12.9 bolts, the trends of mesh size are similar to other grades, the fracture strain is 0.445 at 0.25 mm, 0.46 at 0.50 mm, and 0.50 at 0.75 mm.

Typical failure models of the high-strength bolts simulated with different mesh sizes are shown in Figs. 11-13. It can be seen that all the models experienced visible plastic deformation before fracturing. The red grid area near the fracture surface in this figure is where the equivalent plastic strain is greatest. It can be seen that the equivalent plastic strain at fracture is higher for the lower grade bolts. Noted that changing the mesh size will affect the simulation CPU time. In this paper, the simulation time of the 0.75 mm mesh size model is about 15 min, 0.5 mm is longer, which takes 45–60 min. The model with a 0.25 mm mesh size has a large number of elements, resulting in a simulation time of more than 2 h.

The fracture locus of the uncoupled model is shown inFigs. 14-17. The result shows that 0.75 mm mesh size has the maximum value for all three grades of high strength bolts at uniaxial compression status. The relationship between fracture strain and stress triaxiality for bolts of grades 10.9 and 12.9 shows a similar trend corresponding to different mesh sizes. However, there are some differences for grade 8.8 bolts. In uniaxial tension status, the smallest value of 0.25 mm mesh size is found for three grade bolts, but in other states, the curve of grade 8.8 does not follow this pattern-the smaller mesh size corresponds to the smaller fracture strain. The calibrated weight constant W for the curve of 0.75 is not 0, and it is responsible for the difference about grade 8.8 bolts. The material parameters of the damage model and the fracture strains exposed to uniaxial (UT), plane strain tension (PST), equal biaxial tension (EBT), in-plane shear (SH), uniaxial compression (UC), and equal biaxial compression (EBC) are listed in Table 5.

5. Conclusions

To study the effect of mesh size on ultimate capacity and fracture behavior, an attempt is made with three kinds of mesh size for each grade bolts (including 8.8, 10.9, and 12.9) which engineering stress-engineering strain relationship obtained by refs. [17-20]. The fracture locus of three grade bolts is calibrated based on the mesoscale critical equivalent plastic strain (MCEPS). The following conclusions can be drawn from the present investigation:

(1). In process of calibrating the plasticity curve of the material with a finite element model, the mesh size affects the plastic response of high-strength bolts after the necking. Specifically, in the plastic-dominated zone, it can affect the value of the weight constant W thus making a difference in the plastic curve. In the damage-dominated zone, the mesh size affects the value of maximum equivalent plastic strain $\bar{\varepsilon}^{p}_{d-i}$ and model parameters of damage evolution law B.

(2). Because the mesh size affects the plastic relationship, it will make a difference in the homogenized numerical simulation. It should be noted that changes in the evolution of mesoscale indicator along with the equivalent plastic strain vary depending on the material of high strength bolts, in particular, it affects the value of PST/UT. Meanwhile, the mesh size affects the equivalent plastic strain of the bolts at fracture, and the fracture strain increases with the enlargement of the mesh size. Within the range, the equivalent plastic strain is smaller for higher-grade bolts, and conversely, lower-grade bolts have a larger plastic strain.

(3). The mesh size obviously influenced the fracture locus of high-strength bolts. Generally, smaller mesh sizes imply smaller fracture strain exposed to uniaxial tensile (UT), pure shear (SH), equivalent biaxial tensile (EBT), and plane strain tension (PST).

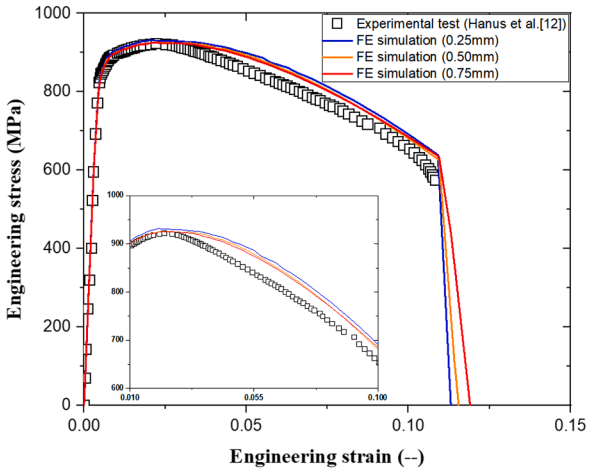

(a) Grade 8.8 bolt

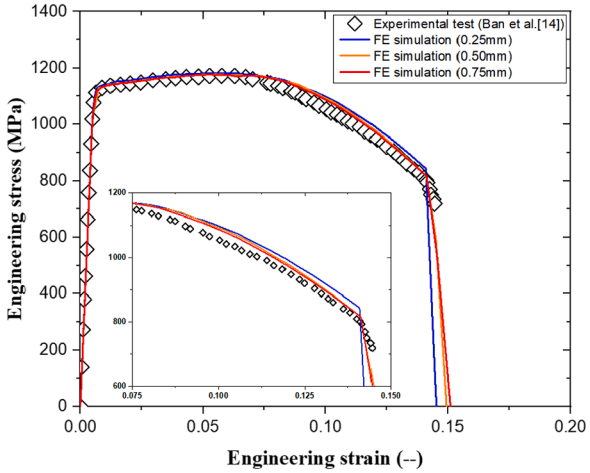

(b) Grade 10.9 bolts

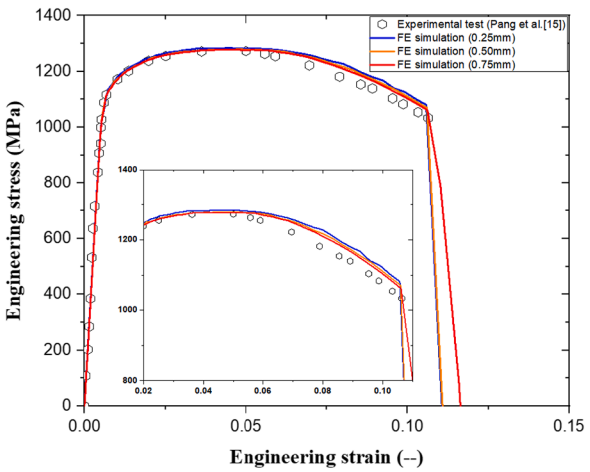

(c) Grade 12.9 bolts

Fig. 10. Calibration of fracture strain exposed to uniaxial loading under different mesh sizes.

Table 4
Summary of fracture strain ($\bar{\varepsilon}_f^p$) exposed to uniaxial loading.

Grade	Mesh size (mm)		
	0.25	0.50	0.75
8.8	0.82	0.83	0.85
10.9	0.70	0.84	0.89
12.9	0.45	0.46	0.50

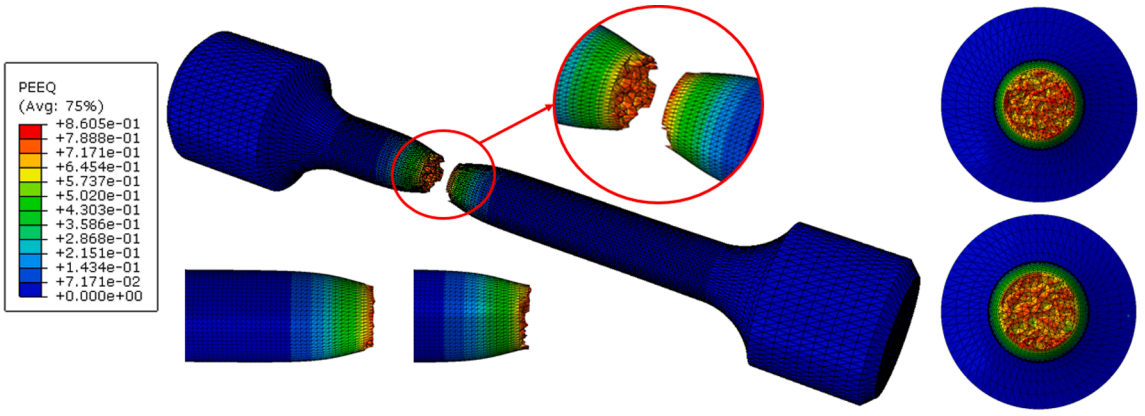

(a) M0.25mm

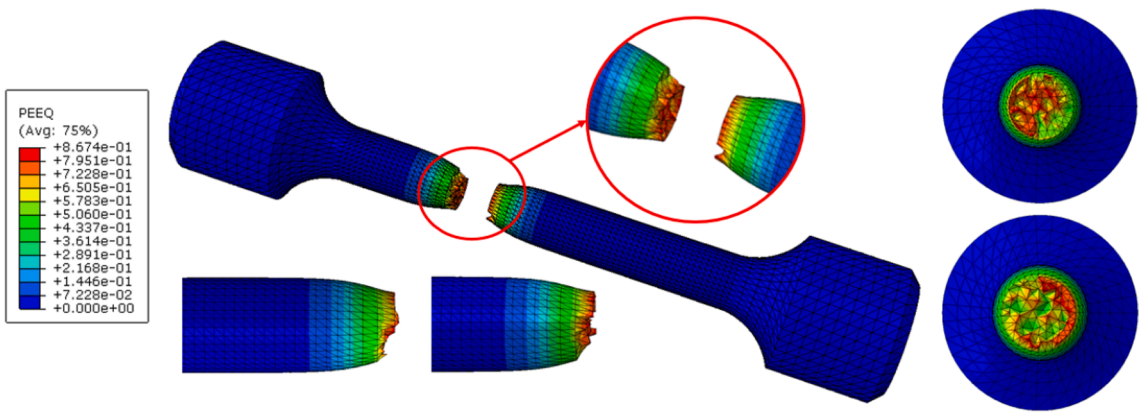

(b) M0.50mm

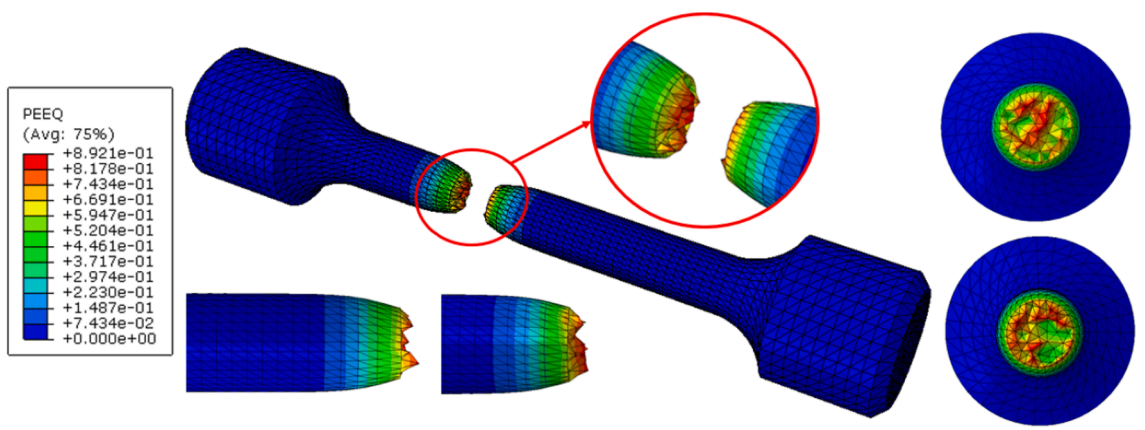

(c) M0.75mm

Fig. 11. Failure mode for FE simulation under various mesh sizes for Grade 8.8 bolt.

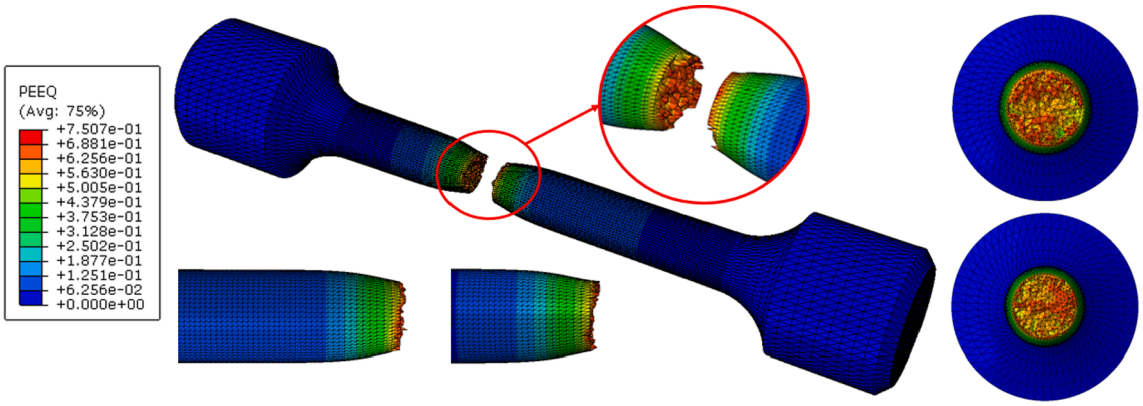

(a) M0.25mm

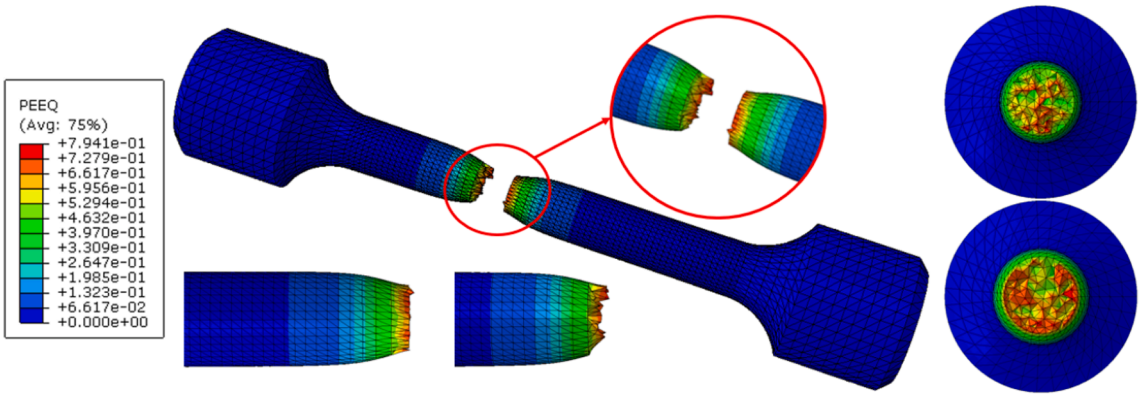

(b) M0.50mm

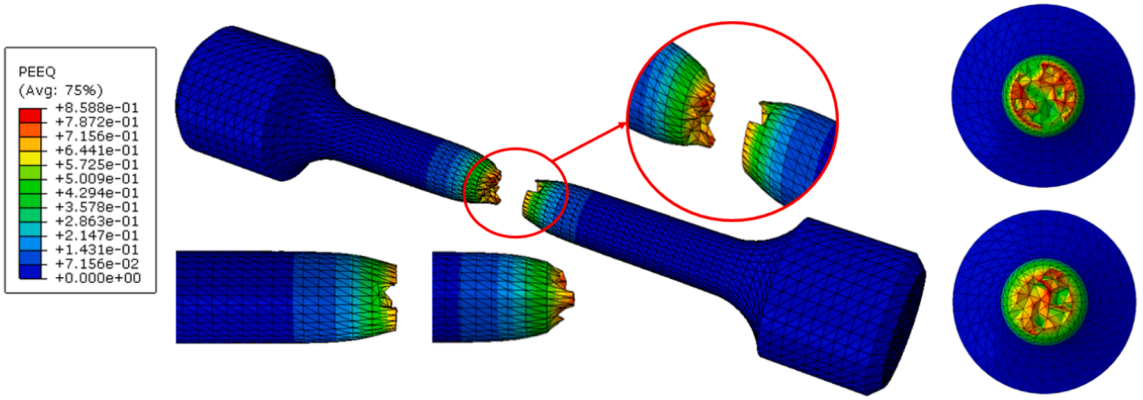

(c) M0.75mm

Fig. 12. Failure mode for FE simulation under various mesh sizes for Grade 10.9 bolt.

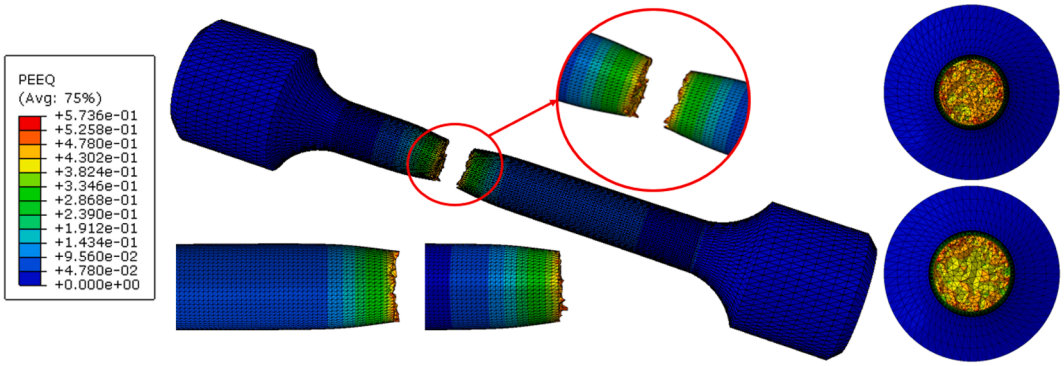

(a) M0.25mm

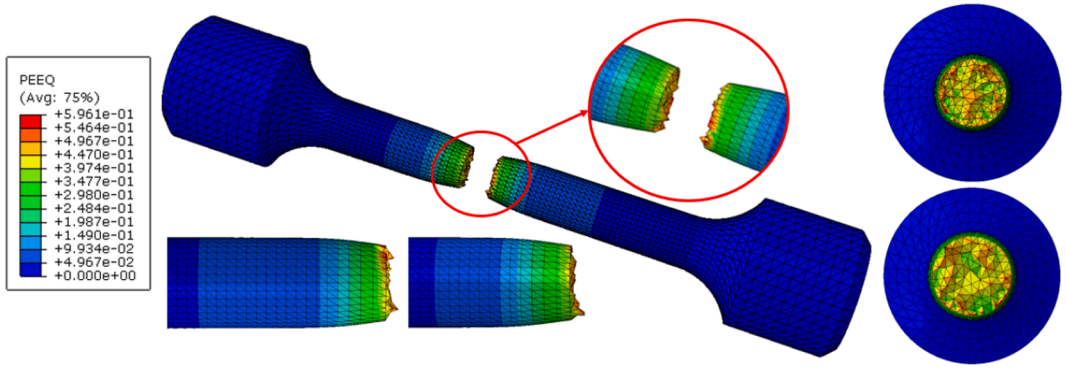

(b) M0.50mm

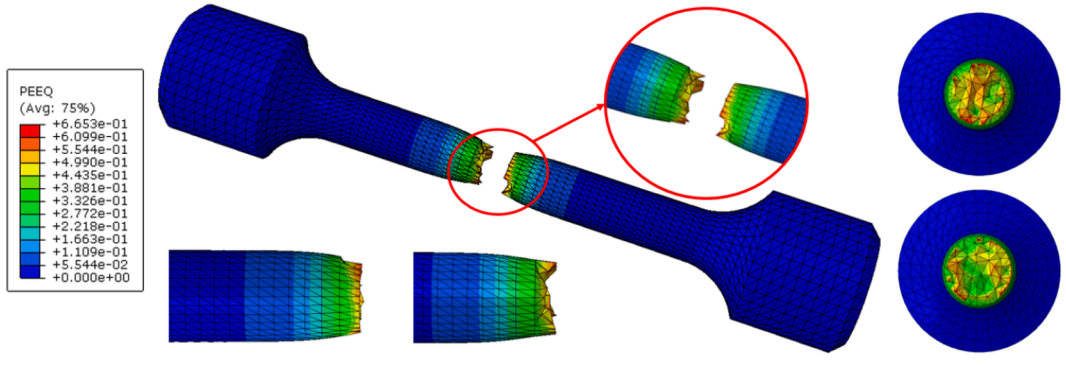

(c) M0.75mm

Fig. 13. The failure mode for FE simulation under various mesh sizes for Grade 12.9 bolt.

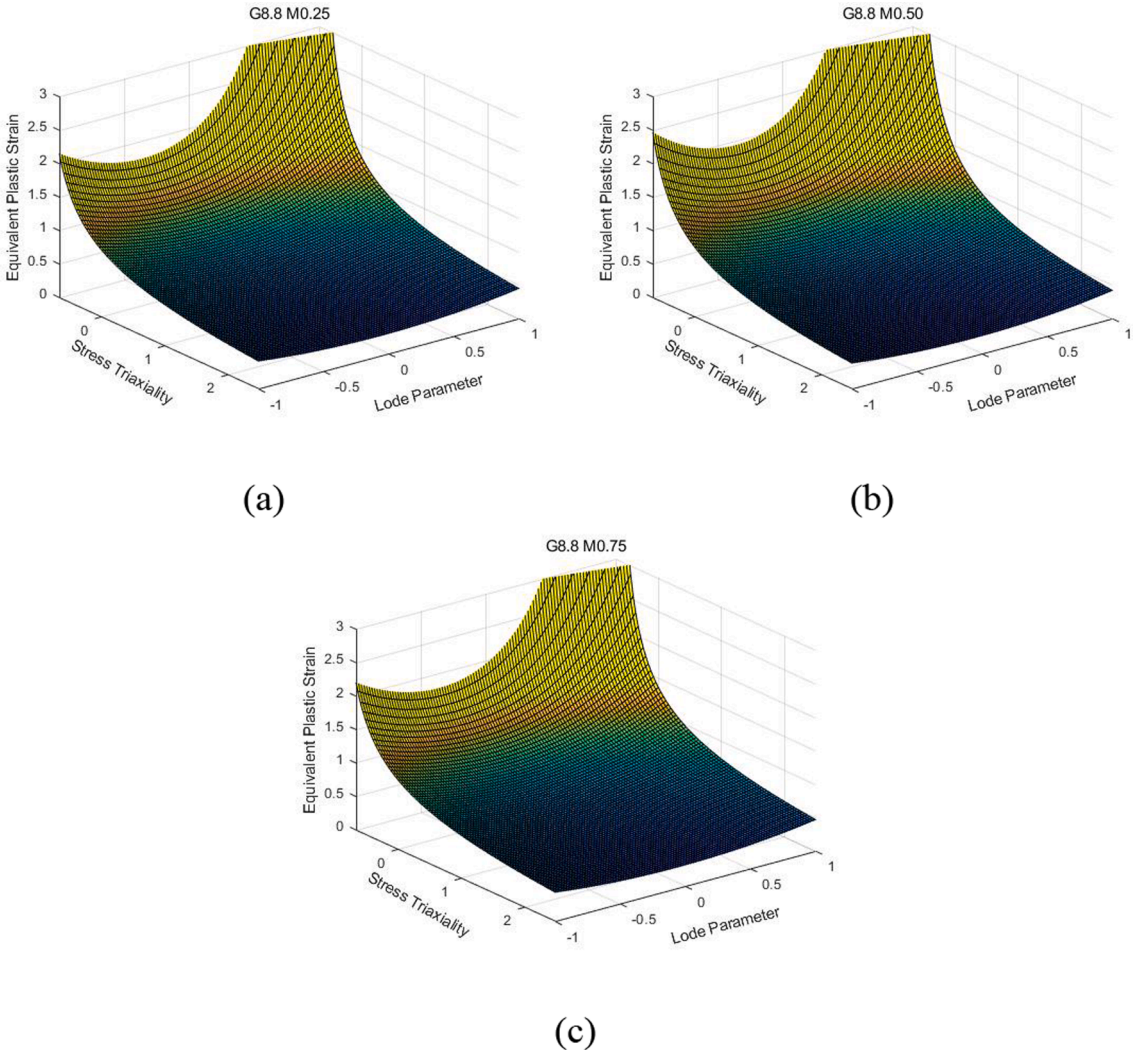

Fig. 14. Fracture locus as a function of the stress triaxiality and lode parameter for Grade 8.8 high-strength bolt.

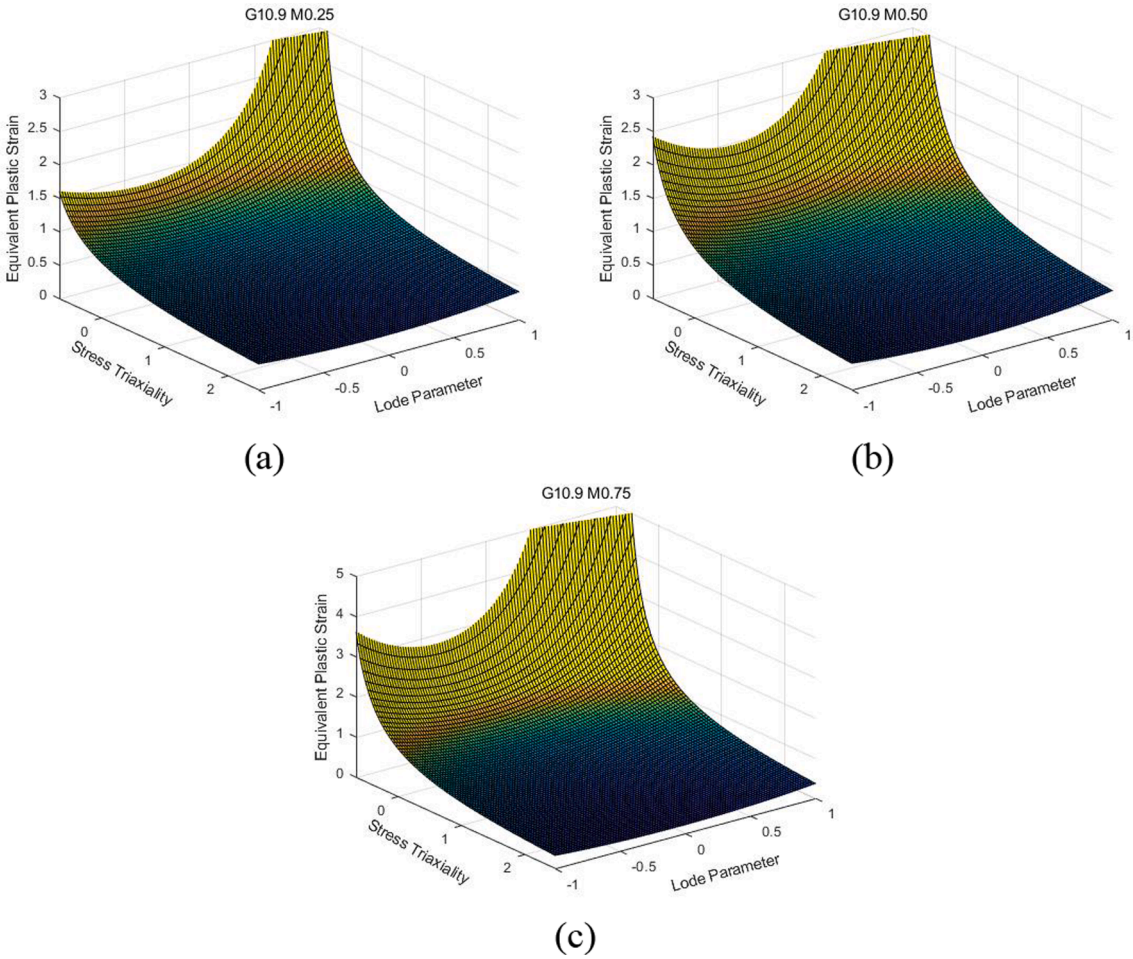

Fig. 15. Fracture locus as a function of the stress triaxiality and lode parameter for Grade 10.9 high-strength bolt.

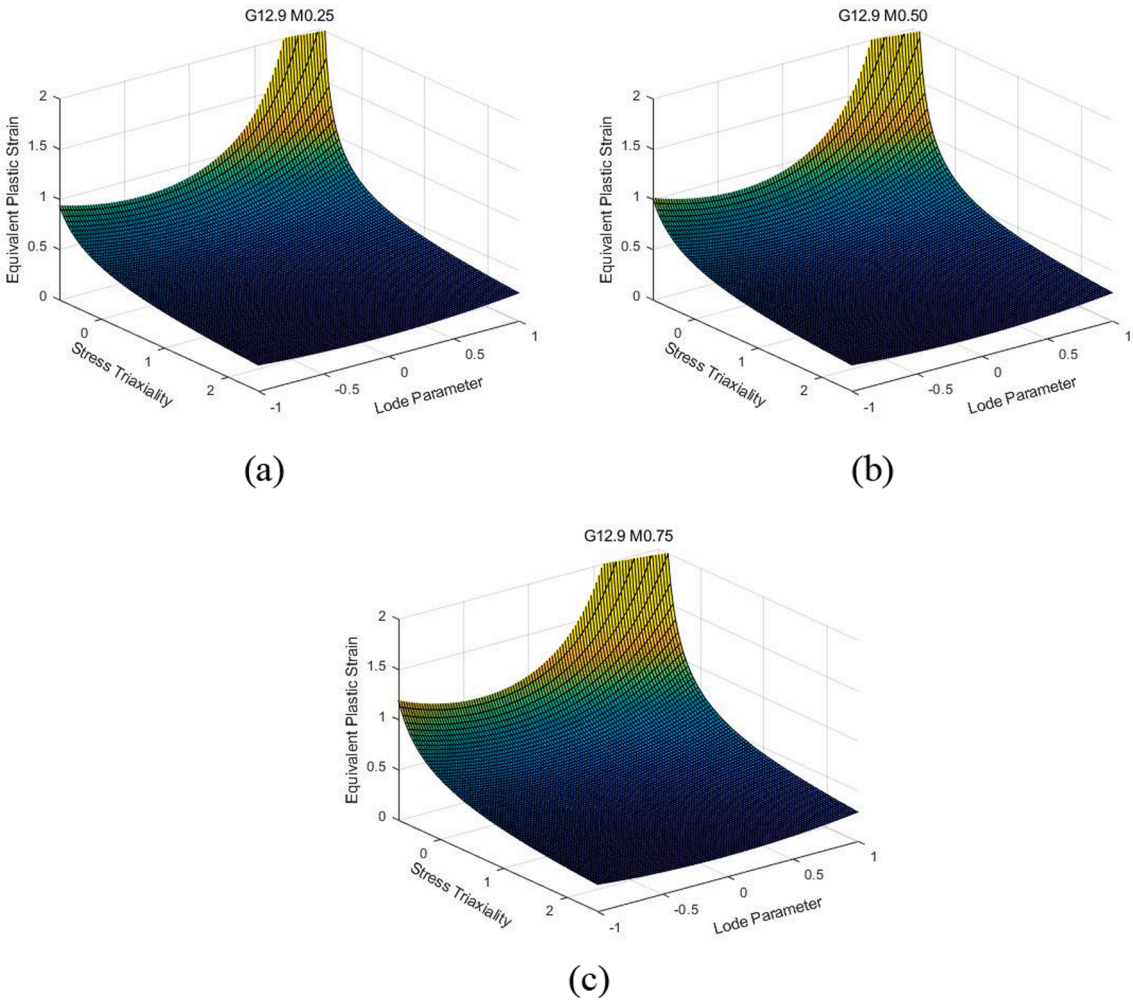

Fig. 16. Fracture locus as a function of the stress triaxiality and lode parameter for Grade 12.9 high-strength bolt.

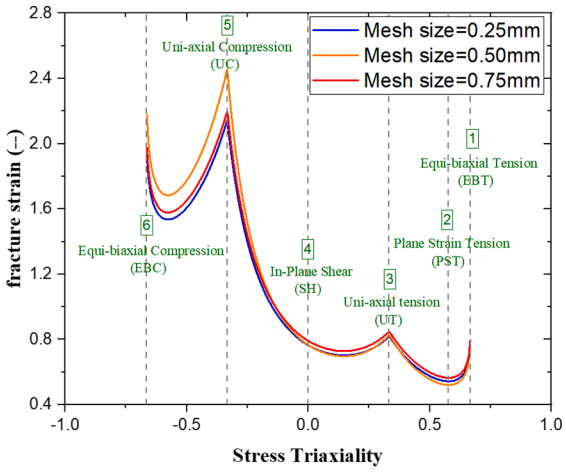

(a) Grade 8.8 bolts

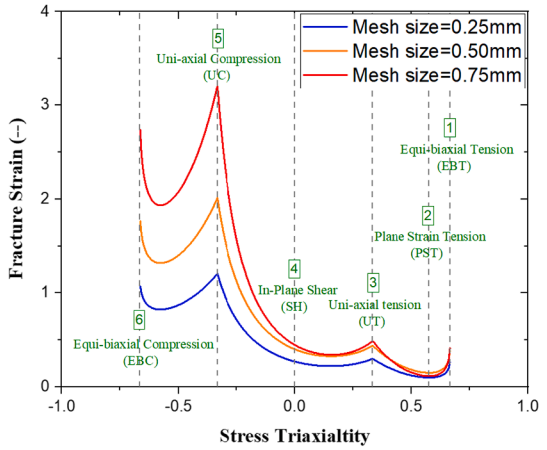

(b) Grade 10.9 bolts

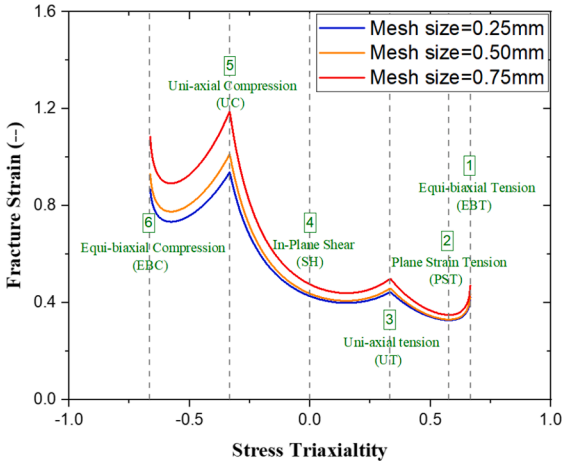

(c) Grade 12.9 bolts

Fig. 17. Fracture strain vs. stress triaxiality exposed to plane stress status.

Table 5
Parameters of damage model and fracture strain at different status.

Item Grade	Mesh Size (mm)	C_1	C_2	C_3	$\bar{\varepsilon}^p_{EBT}$	$\bar{\varepsilon}^p_{PST}$	$\bar{\varepsilon}^p_{UT}$	$\bar{\varepsilon}^p_{SH}$	$\bar{\varepsilon}^p_{UC}$	$\bar{\varepsilon}^p_{EBC}$
8.8	0.25	2.329	0.694	0.820	0.765	0.543	0.820	0.764	2.139	1.926
	0.50	2.635	0.784	0.830	0.767	0.521	0.83	0.766	2.454	2.176
	0.75	2.311	0.686	0.850	0.793	0.566	0.850	0.792	2.191	1.977
10.9	0.25	1.893	0.598	0.700	0.661	0.499	0.7	0.671	1.603	1.472
	0.50	2.355	0.763	0.840	0.782	0.551	0.840	0.801	2.414	2.167
	0.75	3.033	1.011	0.890	0.811	0.515	0.890	0.846	3.602	3.137
12.9	0.25	1.712	0.539	0.445	0.422	0.328	0.445	0.427	0.938	0.867
	0.50	1.860	0.570	0.460	0.435	0.331	0.460	0.438	1.011	0.930
	0.75	2.003	0.626	0.500	0.470	0.350	0.500	0.476	1.188	1.085

Declaration of Competing Interest

The authors declare that they have no known competing financial interests or personal relationships that could have appeared to influence the work reported in this paper.

Acknowledgments

This research was funded by SCEGC-XJTU Joint Research Center (Grant Number: 20211177-ZKT10) for Future City Construction and Management Innovation.

References

[1] M. Veljkovic, B. Johansson, Design of hybrid steel girders, J. Constr. Steel Res. 60 (3–5) (2004) 535–547.
[2] Y. Du, Z. Chen, J.Y.R. Liew, M.X. Xiong, Rectangular concrete-filled steel tubular beam-columns using high-strength steel: Experiments and design, J. Constr. Steel. Res. 131 (2017) 1–18, https://doi.org/10.1016/j.jcsr.2016.12.016.
[3] H. Zhao, Y. Yuan, Experimental studies on composite beams with high-strength steel and concrete, Steel Compos. Struct. 10 (5) (2010) 373–383.
[4] X.-L. Zhao, Section capacity of very high strength (VHS) circular tubes under compression, Thin-Walled Struct. 37 (3) (2000) 223–240.
[5] R. Bjorhovde, Development and use of high performance steel, J. Constr. Steel Res. 60 (3–5) (2004) 393–400.
[6] L. Yang, B. Yang, G. Yang, Y. Xu, S. Xiao, S. Jiang, J. Chen, Analysis of competitive failure life of bolt loosening and fatigue, Eng. Fail. Anal. 129 (2021) 105697.
[7] Gao D, Yao W, Wu T. Failure analysis on the axial-connected bolts of the thin-walled cylinder under random vibration loading. Engineering Failure Analysis.
[8] E.P. Stoddart, M.P. Byfield, J.B. Davison, A. Tyas, Strain rate dependent component based connection modelling for use in non-linear dynamic progressive collapse analysis, Eng. Struct. 55 (2013) 35–43.
[9] G. Culache, M.P. Byfield, N.S. Ferguson, A. Tyas, Robustness of beam-to-column end-plate moment connections with stainless steel bolts subjected to high rates of loading, J. Struct. Eng. 143 (6) (2017) 04017015.
[10] A.S. Standards Australia, 4100-1998: Steel, structures (2016) 99–101SAI 1999.
[11] GB/T 3098.1—2010, Mechanical properties of fasteners -bolts ,screws and studs, Beijing, 2011.
[12] Eurocode 3, Design of Steel Structures, Part 1.8, Design of joints, BS EN 1993-1-8, vol.2005, UK, London, 2005.
[13] ANSI/AISC-360-16, Specification for structural steel buildings, Chicago: AISC, 2016.
[14] Sterling, G.H. and Fisher, J.W. (1964). "Tests of A490 Bolts." Fritz Engineering Lab. Report, No. 288.15, Lehigh University. Standards Australia, AS 4100-1998: Steel structures, 2016.
[15] R.S. Nair, P.C. Birkemoe, W.H. Munse, High strength bolts subject to tension and prying, J. Struct. Div., ASCE 100 (2) (1974) 351–372.
[16] Amrine, J.J. and Swanson, J.A. (2004), "Effects of variable pretension on the behavior of bolted connections with prying," Engineering Journal, American Institute of Steel Construction, 3rd Quarter, 2004.
[17] Pang X-P, Hu Y, Tang S-L, et al. Physical properties of high-strength bolt materials at elevated temperatures. Results in Physics. 2019;13. 2019.102156.
[18] H. Ban, Q. Yang, Y. Shi, Z. Luo, Constitutive model of high-performance bolts at elevated temperatures, Eng. Struct. 233 (2021) 111889.
[19] D. Li, B. Uy, J. Wang, Y. Song, Behaviour and design of high-strength Grade 12.9 bolts under combined tension and shear, J. Constr. Steel Res. 174 (2020) 106305.
[20] F. Hanus, G. Zilli, J.-M. Franssen, Behaviour of Grade 8.8 bolts under natural fire conditions—Tests and model, J. Constr. Steel Res. 67 (8) (2011) 1292–1298, https://doi.org/10.1016/j.jcsr.2011.03.012.
[21] A.A. Hedayat, E.A. Afzadi, A. Iranpour, Prediction of the bolt fracture in shear using finite element method, Structures 12 (2017) 188–210.
[22] M. D'Anello, D. Cassiano, R. Landolfo, Simplified criteria for finite element modelling of European preloadable bolts, Steel and Composite Structures 24 (6) (2017) 643–658.
[23] J.P. Mersch, J.A. Smith, E.P. Johnson, A case study for the low fidelity modeling of threaded fasteners subject to tensile loadings at low and high strain rates. American Society of Mechanical Engineers, Pressure Vessels and Piping Division (Publication) PVP, [s. l.], v. 2, [s. d.]. DOI 10.1115/PVP201765118. Disponível em:.
[24] Y. Song, J. Wang, B. Uy, D. Li, Experimental behaviour and fracture prediction of austenitic stainless steel bolts under combined tension and shear, J. Constr. Steel Res. 166 (2020) 105916.
[25] F. Schauwecker, et al., Investigation of the failure behavior of bolted connections under crash loads and a novel adaption to an enhanced abstracted bolt model, in 15th International LS-DYNA Users Conference, Detriot, Michigan, 2018.
[26] Xin H, Li J, Veljkovic M,et al. Evaluating the strength of grade 10.9 bolts subject to multiaxial loading using the micromechanical failure index: MCEPS, STEEL CONSTRUCTION-DESIGN AND RESEARCH, February,2022.
[27] Y. Bai, T. Wierzbicki, Application of extended Mohr–coulombcriterion to ductile fracture, Int J Fract. 161 (1) (2010) 1–20.
[28] C.C. Roth, D. Mohr, Effect of strain rate on ductile fracture initiation in advanced high strength steel sheets: experiments and modeling, Int J Plast. 56 (2014) 19–44.
[29] S.J. Marcadet, D. Mohr, Effect of compression–tension loading reversal on the strain to fracture of dual phase steel sheets, Int. J. Plast. 72 (2015) 21–43.
[30] H. Xin, M. Veljkovic, J.A.F.O. Correia, F. Berto, Ductile fracture locus identification using mesoscale critical equivalent plastic strain, Fatigue Fract. Eng. Mater. Struct. 44 (5) (2021) 1292–1304.

[31] H. Xin, J.A.F.O. Correia, M. Veljkovic, F. Berto, Fracture parameters calibration and validation for the high strength steel based on the mesoscale failure index, Theor. Appl. Fract. Mech. 112 (2021) 102929.
[32] H. Xin, M. Veljkovic, Evaluation of high strength steels fracture based on uniaxial stress-strain curves, Eng. Fail. Anal. 120 (2021) 105025.
[33] Y. Lou, J.W. Yoon, H. Huh, Modeling of shear ductile fracture considering a changeable cut-off value for stress triaxiality, IntJ Plast. 54 (2014) 56–80.
[34] Y. Ling, Uniaxial true stress-strain after necking, AMP J. Technol. 5 (1996) 37–48.
[35] Haoyun Tu, Numerical Simulation and Experimental Investigation of the Fracture Behaviour of an Electron Beam Welded Steel Joint. Springer, 2018. Accessed March 15, 2022.
[38] Y. Lou, H. Huh, S. Lim, K. Pack, New ductile fracture criterion for prediction of fracture forming limit diagrams of sheet metals, Int. J. Solids Struct. 49 (25) (2012) 3605–3615.